

# Journal of Astronomical Telescopes, Instruments, and Systems

AstronomicalTelescopes.SPIEDigitalLibrary.org

## **Fine-pointing performance and corresponding photometric precision of the Transiting Exoplanet Survey Satellite**

Tam Nguyen  
Edward Morgan  
Roland Vanderspek  
Alan Levine  
Miranda Kephart  
James Francis  
Joseph Zepetis  
Kerri Cahoy  
George Ricker

**SPIE.**

Tam Nguyen, Edward Morgan, Roland Vanderspek, Alan Levine, Miranda Kephart, James Francis, Joseph Zepetis, Kerri Cahoy, George Ricker, "Fine-pointing performance and corresponding photometric precision of the Transiting Exoplanet Survey Satellite," *J. Astron. Telesc. Instrum. Syst.* **4**(4), 047001 (2018), doi: 10.1117/1.JATIS.4.4.047001.

# Fine-pointing performance and corresponding photometric precision of the Transiting Exoplanet Survey Satellite

Tam Nguyen,<sup>a,b,\*</sup> Edward Morgan,<sup>a</sup> Roland Vanderspek,<sup>a</sup> Alan Levine,<sup>a</sup> Miranda Kephart,<sup>a</sup> James Francis,<sup>a</sup> Joseph Zapetis,<sup>a</sup> Kerri Cahoy,<sup>b</sup> and George Ricker<sup>a</sup>

<sup>a</sup>Massachusetts Institute of Technology, Kavli Institute of Astrophysics and Space Research, Cambridge, Massachusetts, United States

<sup>b</sup>Massachusetts Institute of Technology, Department of Aeronautics and Astronautics, Cambridge, Massachusetts, United States

**Abstract.** The Transiting Exoplanet Survey Satellite (TESS) is an MIT-led, NASA-funded Explorer-class planet finder launched in April 2018. TESS will carry out a 2-year all-sky survey with the primary goal of detecting small transiting exoplanets around bright and nearby stars. The TESS instrument consists of four wide-field cameras in a stacked configuration, providing a combined field of view of  $24 \text{ deg} \times 96 \text{ deg}$  that spans approximately from the ecliptic plane to the ecliptic pole. In order to achieve the desired photometric precision necessary for the mission, TESS uses the instrument cameras as star trackers during fine-pointing mode to enhance attitude accuracy and stabilization for science operations. We present our approach in quantifying the expected performance of the fine-pointing system and assessing the impact of pointing performance on the overall photometric precision of the mission. First, we describe the operational details of the fine-pointing system with the science instrument being used for star-tracking. Next, we present the testing framework used to quantify the attitude determination performance of the system and the expected attitude knowledge accuracy results, both in coarse-fine pointing hand-off and in nominal fine-pointing conditions. By combining simulations of the instrument and the spacecraft bus, we quantify the closed-loop fine-pointing stability performance of the system in nominal science operations as well as in the case of camera unavailability due to Earth/Moon interference. Finally, we assess the impact of platform pointing stability on the photometric precision of the system using detailed system modeling and discuss the applicability of mitigation techniques to reduce the effect of jitter on TESS science data. © The Authors. Published by SPIE under a Creative Commons Attribution 3.0 Unported License. Distribution or reproduction of this work in whole or in part requires full attribution of the original publication, including its DOI. [DOI: [10.1117/1.JATIS.4.4.047001](https://doi.org/10.1117/1.JATIS.4.4.047001)]

Keywords: Transiting Exoplanet Survey Satellite; fine-pointing; photometric precision.

Paper 18017 received Mar. 17, 2018; accepted for publication Jul. 26, 2018; published online Sep. 4, 2018.

## 1 Introduction

### 1.1 Transiting Exoplanet Survey Satellite

The Transiting Exoplanet Survey Satellite (TESS) is a 2-year all-sky survey mission looking for transiting exoplanets around bright and nearby stars.<sup>1,2</sup> TESS is the natural successor to the highly-successful Kepler mission, which has enabled significant advancements in exoplanet sciences.<sup>3</sup> While Kepler has succeeded in detecting thousands of exoplanets, many Kepler stars are too faint for detailed follow-up observations.<sup>1</sup> TESS aims to discover small transiting planets around bright and nearby stars such that existing and future ground and space telescopes, like the James Webb Space Telescope (JWST), can be used to study the mass of the planets and their atmospheric properties. TESS will monitor hundreds of thousands of stars and collect differential time-series photometry, projecting to detect thousands of nearby exoplanets, including some in the habitable zone.<sup>1,2,4</sup> The TESS mission is funded by NASA as an Explorer-class planet-finder. The TESS payload and spacecraft are developed primarily by MIT and Orbital ATK, respectively, along with other collaborators. TESS was launched on a SpaceX Falcon 9 from Cape Canaveral, FL on April 18, 2018.

The orbit of TESS is a high-Earth, 2:1 lunar-resonant orbit, a low-cost, and stable orbit option that is capable of providing a relatively unobstructed view of the celestial sphere.<sup>5</sup> The final elliptical orbit has a 13.7-day period with a nominal perigee at  $17 R_{\oplus}$  and apogee at  $59 R_{\oplus}$ , achieved by a series of apogee-raising and perigee-raising burns and a lunar gravity assist.<sup>2,5</sup> The mission operational modes include the low altitude house-keeping operations (LAHO) near perigee and the high altitude science operations (HASO) for the remaining portion of the orbit. During LAHO, which lasts  $\sim 16$  h, both Ka-band science data downlink and S-band uplink and downlink for telemetry and commands are enabled. During HASO, the instrument's field of view ( $24 \text{ deg} \times 96 \text{ deg}$ ) spans approximately the ecliptic plane to the ecliptic pole, generally in the anti-Sun direction, monitoring the brightness of tens of thousands of target stars of interest. Over the course of the mission, TESS will observe a total of 26 sectors, including 13 in the Northern Hemisphere and 13 in the Southern Hemisphere, where each sector lasts 27.4 days.<sup>1,2</sup>

The TESS instrument, developed primarily by MIT and MIT Lincoln Laboratory, consists of an Alternate Data Handling Unit (ADHU) and four identical refractive cameras. The ADHU processes image data from the cameras at high speed and serves as an interface between the cameras and the spacecraft bus. Each camera consists of a seven-element lens system and a CCD detector assembly. The lens system is an  $f/1.4$  custom design

\*Address all correspondence to: Tam Nguyen, E-mail: [tamz@mit.edu](mailto:tamz@mit.edu)

with an aperture of 10.5 cm.<sup>1,2</sup> The focal plane array assembly is a combination of four back-illuminated MIT Lincoln Laboratory CCID-80 devices.<sup>6</sup> The effective imaging array is  $4096 \times 4096$  pixels<sup>2</sup>, where each pixel is  $15 \times 15 \mu\text{m}^2$ . Each camera provides an effective field of view of  $24 \text{ deg} \times 24 \text{ deg}$  with a wavelength range of 600 to 1000 nm.<sup>1,2</sup>

The TESS spacecraft bus is based on the LEOStar-2, a flexible high-performance platform with space-heritage developed by Orbital ATK. Previous missions that have used the LEOStar-2 bus include SORCE, GALEX, AIM, NuSTAR, and others.<sup>7</sup> The TESS spacecraft total launch mass is 350 kg with deployed configuration dimensions of  $\sim 3.9 \text{ m} \times 1.5 \text{ m}$ .<sup>7</sup> The spacecraft bus is capable of providing 400 W (end of life) from two single-axis solar arrays. The Ka-band antenna can achieve a data downlink rate of 100 Mbps near perigee. The spacecraft attitude control system provides three-axis stabilization using a two-headed star tracker, an inertial reference unit, and a four-wheel zero-momentum system.<sup>7</sup>

### 1.2 TESS Attitude Determination and Control System

TESS Attitude Determination and Control System (ADCS) ensures the spacecraft and instrument achieve the pointing performance necessary to meet the mission requirements in each operation mode. The mission ADCS modes include Sun-pointing, deep space network (DSN) pointing, coarse pointing, and fine pointing. Table 1 shows the sensors and actuators used to achieve each pointing mode. The Sun-pointing and DSN-pointing modes ensure basic functionality of the power and communication subsystems. The coarse and fine-pointing modes are primarily used to achieve the desired attitude of the spacecraft during science operations. Figure 1 shows the spacecraft and instrument coordinate system and the desired Northern-Hemisphere science operation attitude, with the four cameras' boresights pointing generally in the anti-Sun direction and spanning approximately from the ecliptic plane to the ecliptic pole.

The coarse pointing mode uses two orthogonal body-mounted star trackers and an inertial reference unit for attitude

knowledge and reaction wheels for actuation. The coarse-pointing requirement is 120 arc sec ( $3\sigma$ ), fulfilled by the sensing-limited spacecraft-only ADCS. After coarse pointing is achieved, the fine-pointing system is activated, which utilizes the instrument cameras as attitude sensors and the spacecraft reaction wheels as actuators. In order to improve the pointing performance of the system, the fine-pointing system is implemented with the use of the instrument cameras in the loop as star trackers. The attitude knowledge accuracy required from the instrument cameras for coarse-to-fine pointing hand-off is 20 arc sec. The fine-pointing noise equivalent angle requirement of the instrument cameras during nominal fine-pointing conditions is  $<0.6 \text{ arc sec}$  ( $3\sigma$ ) about the cross-boresight axes and  $<4.2 \text{ arc sec}$  ( $3\sigma$ ) about the roll axis.<sup>8</sup> The stability requirement for the system during science operation is  $<0.06 \text{ arc sec}$  ( $3\sigma$ ) per hour and  $<2 \text{ arc sec}$  ( $3\sigma$ ) per minute.<sup>9</sup>

The pointing requirements were derived based on the required systematic error contribution limit of 60 parts per million (ppm) in stellar photometry for stars brighter than eighth magnitude at 1-h cadence, necessary to achieve the desired planet-yield performance of the mission.<sup>4</sup> Of the 60 ppm requirement on systematic error residual, 30 ppm are allocated to jitter-induced photometric error. The brightness of a star is measured by summing the charge collected in a fixed set of pixels (the photometric aperture). As the spacecraft jitters, the stellar point-spread function (PSF) moves with respect to its fixed photometric aperture; as a result, the amount of charge collected in that aperture varies. This variation is caused by the star's PSF moving in and out of the fixed photometric aperture as well as the different weighting of pixel values in the PSF due to pixel-to-pixel quantum efficiency variations.

The fine-pointing scheme is summarized in Fig. 2. Guide-star tables, consisting of the predicted locations of the guide-star centroids for the desired spacecraft attitude, and guide-star centroiding parameter files are uplinked to the spacecraft. This information is passed to the instrument ADHU through the spacecraft Master Avionics Unit (MAU). The ADHU reads out the guide-star "postage stamps" with 2-s integrations from one camera at a time, sequencing through the four cameras asynchronously. The ADHU then performs background subtraction and runs a centroiding algorithm over the predefined windows for the guide stars to estimate their locations. The differences between the predicted and measured guide-star locations in each camera are used to compute a rotation matrix, which represents the pointing offset of the camera boresight relative to the desired camera pointing direction. The rotation matrices are converted into error quaternions for each camera and sent to the MAU every 2 s. The MAU receives updated error quaternions at 2 Hz, from one camera at a time with an offset of 0.5 s. The spacecraft attitude control system implements filtering techniques on the error quaternions received from the ADHU and corrects for the pointing error by using body-mounted reaction wheels, completing a closed-loop system.

**Table 1** ADCS sensors and actuators used in each pointing mode (credit: Orbital ATK).

	Sun pointing	DSN pointing	Coarse pointing	Fine pointing
<b>Sensors</b>				
Coarse sun sensors	×			
Star trackers		×	×	
Instrument cameras				×
Inertial reference unit	×	×	×	
<b>Actuators</b>				
Reaction wheels	×	×	×	×

### 1.3 Paper Outline

In this paper, we focus on assessing the performance of the instrument in the loop for fine-pointing and the corresponding impact of pointing errors on the mission's photometric precision. In Sec. 2, we present operational details of the use of the instrument cameras as star trackers in fine-pointing mode, including the attitude determination algorithm implemented in the ADHU and the guide-star selection method. In Sec. 3,

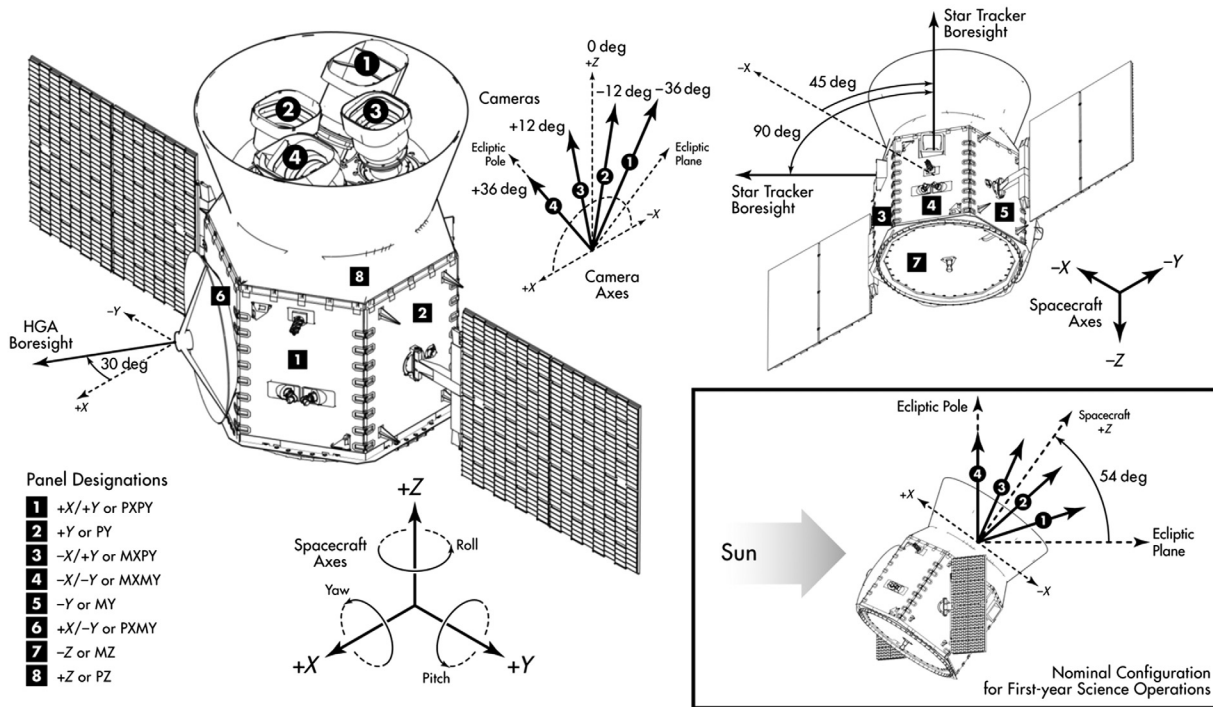


**Fig. 1** TESS ADCS coordinate system and nominal Northern-Hemisphere science operation attitude (credit: Orbital ATK).

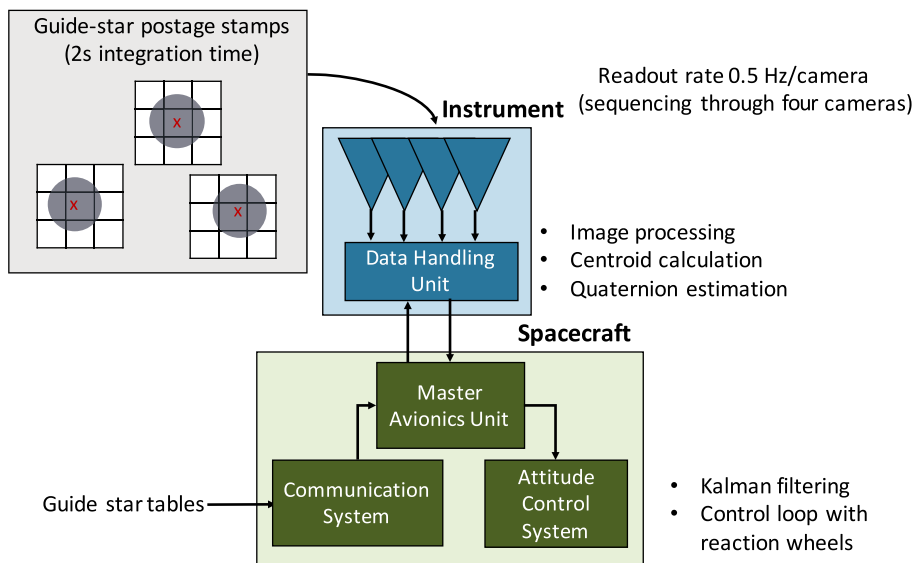


**Fig. 2** Overview of the TESS fine-pointing system.

we present a testing framework used to validate the attitude determination software implementation and report the expected attitude determination accuracy of the instrument cameras, both during coarse-to-fine pointing hand-off and during nominal fine-pointing disturbances. In Sec. 4, we present the closed-loop fine-pointing performance by combining the instrument model with the spacecraft dynamic model as provided by Orbital ATK. Next, we present the expected photometric precision achieved by the system, given the current fine-pointing performance predictions in Sec. 5. Finally, we summarize the results presented in this paper and discuss future directions in Sec. 6.

## 2 Instrument Cameras Star-Tracking System

### 2.1 Attitude Determination Method Overview

The instrument cameras are used effectively as star trackers during fine-pointing mode as previously described in Sec. 1.2. At the beginning of each observation sector, a set of guide-star tables, specifying the pixel locations of the guide stars for each camera, is uplinked to the spacecraft. The instrument computer (ADHU) retrieves the guide-star “postage-stamps” centered at each predicted guide-star location. The size of the guide-star postage stamps is configurable and is set by default to be

$15 \times 15$  pixels<sup>2</sup>. If the brightest pixel in the postage-stamp is not within the predefined region-of-interest (a portion of the postage-stamp), the guide-star position is set to the center of the brightest pixel. In the case where the brightest pixel is in the region-of-interest, the ADHU computes the photometric centroid position of the guide star by using a standard first-moment centroiding method using the pixel values in the specified region-of-interest after background subtraction. The measured guide-star centroids and the reference guide-star positions as indicated in the guide-star tables are used to compute the best-fit Euler angles, representing the actual spacecraft attitude relative to the desired spacecraft attitude.

When a guide-star position unit vector in the camera frame  $(x_i, y_i, z_i)$  is rotated by small Euler angles  $\phi$ ,  $\theta$ , and  $\psi$ , the theoretical resulting unit vector  $(x'_i, y'_i, z'_i)$  can be represented by Eqs. (1)–(3) where small-angle approximations have been applied. The goal of the attitude determination algorithm is to find the Euler angles  $\theta$ ,  $\phi$ , and  $\psi$  that minimize the cost function  $S$ , shown in Eq. (4), where  $(x'_{im}, y'_{im})$  indicates the measured position of guide star  $i$ . The optimization problem can be solved analytically by differentiation with respect to the Euler angle parameters.<sup>10</sup> The set of Euler angle solutions is converted into a single error quaternion for each camera, which is sent to the MAU in the spacecraft ADCS for further filtering and pointing correction using body-mounted reaction wheels.

$$x'_i = x_i + \phi y_i - \psi z_i, \quad (1)$$

$$y'_i = -\phi x_i + y_i + \theta z_i, \quad (2)$$

$$z'_i = \psi x_i - \theta y_i + z_i, \quad (3)$$

$$S(\theta, \phi, \psi) = \sum_{i=1}^N (x'_{im} - x'_i)^2 / \sigma_{xi}^2 + (y'_{im} - y'_i)^2 / \sigma_{yi}^2. \quad (4)$$

## 2.2 Guide-Star Selection

During each observation sector,  $\sim 200$  guide stars are selected for each camera based on a set of criteria on stellar properties,

field angles, and proximity to other bright objects. In this section, we present our approach in identifying field position, magnitude, and proximity filtering criteria in the guide-star selection process. Proper motion and variability were assessed and concluded to not be major contributors to guide-star acquisition and centroid stability in this case.

### 2.2.1 Field position and magnitude selection

In order to find the range of stellar magnitudes and field positions suitable for guide stars, a framework was created to assess the centroid accuracy of simulated star images. The candidate guide-star images were simulated by querying high-resolution PSFs, binning the PSF according to the pixel size, and injecting noise into the pixelated image. The framework made use of an existing PSF database, developed through detailed modeling based on ray-tracing methods and thermal vacuum optical testing results of the flight cameras.<sup>11</sup> The simulated star image is then moved according to a  $11 \times 11$  grid pattern over the span of 1 pixel. We compare the measured centroid offsets with the true offsets of the PSF at each of the 121 subpixel grid data points to assess the likely accuracy in centroid calculation of a star of interest.

First, we assess the general trend of centroid error of stars across the field of view by using PSFs from 169 independent field positions across one detector quadrant with no additional noise added. Figure 3(a) shows the worst case centroid error results of simulated stars as a function of field angles for one detector quadrant. It can be observed that on-axis stars have elevated centroid error. This effect is due to the small PSF size of on-axis stars relative to the pixel size, causing undersampling and, consequently, degradation in centroid accuracy. Corner stars also have slightly degraded centroiding accuracy due to the size of the PSF extending beyond the predefined centroiding region. It can be seen that the optimal region for guide-star selection is a ring-shape region with no on-axis or corner stars.

To assess the centroid errors of guide stars taking into account stellar magnitudes, we implement the framework presented above with stellar shot noise, background noise, and detector noise sources. The centroid errors are collected at

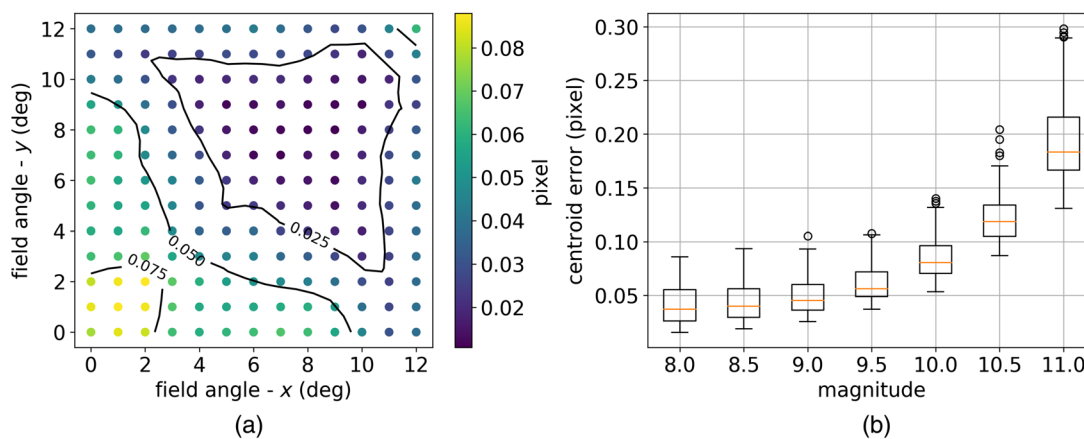


**Fig. 3** (a) Centroid error of noiseless PSF at different field positions over one detector quadrant. (b) Centroid error for stars with magnitude of 8 to 11. The box at each stellar magnitude presents the distribution of centroid errors for stars at different field positions, showing the median (red line), quartiles (box), range of data (whiskers), and outliers (circles).

different field positions at each stellar magnitude, ranging from 8th to 11th magnitude. Figure 3(b) shows the results in box plot format, where the median (red line), quartiles (box), range of data (whiskers), and outliers (circles) are presented at each stellar magnitude. The magnitude range of interest is above 8 since saturation occurs at magnitude of 7.8. The results show that the centroid error distribution remains comparable for stellar magnitudes between 8 and 9 and starts to increase at magnitude 9.5 before growing significantly at magnitude 10 and beyond. For this reason, the desirable magnitude range for guide stars was set to be between 8 and 9 and can be extended to 9.5 if additional stars are needed for the observation sector. Since the centroid error with relevant noise sources included is expected to be  $<0.1$  pixel, sufficient to achieve the desired noise-equivalent angle, field position filtering remains optional for operation.

### 2.2.2 Proximity filtering

Proximity filtering is necessary to ensure that the guide stars can be acquired efficiently during coarse-to-fine pointing hand-off and to reduce interference from other neighboring stars on the centroid positions of the guide stars. During acquisition, the system relies on the brightest pixel in each guide-star postage stamp to belong to the guide star itself. For this reason, a good guide-star candidate needs to be sufficiently far apart from other bright objects (brighter than 11th magnitude). In the case of saturated objects, additional margin is needed in the column direction. In addition to proximity to bright objects, we also eliminate stars with variable stars as neighbors, as the fluctuation in brightness of the neighbor star would cause the centroid position of the guide star to vary over time even with stable pointing. Finally, we ensure that the guide star is within the science region of the CCDs with margin and away from undesirable CCD regions such as straps. The proximity filtering criteria parameters are summarized in Table 2.

## 3 Attitude Determination Performance of the Instrument Cameras

### 3.1 Testing Framework

A framework is created to test the performance of the attitude determination algorithms described in Sec. 2.1 as implemented in the flight ADHU software. A block-diagram summary of the testing framework is shown in Fig. 4. As described in Sec. 1.2, the ADHU computes the fine-pointing quaternion using images from the cameras and a list of predetermined guide stars. The method consists of two main steps: (1) computing the guide-

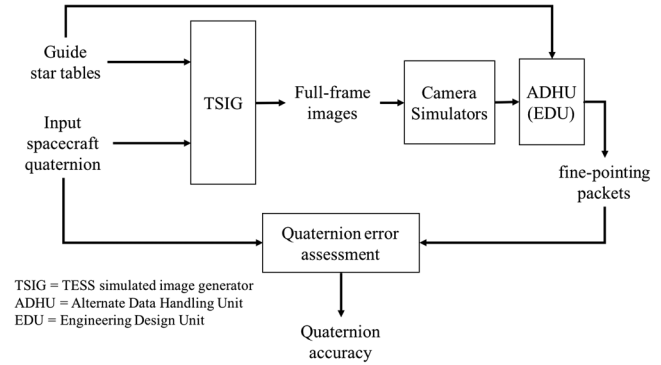


Fig. 4 Attitude determination performance testing framework.

star centroids and (2) computing a quaternion based on the measured and desired centroids. In this framework, the TESS simulated image generator (TSIG) was used to produce a series of 2-s images from all four cameras following a spacecraft scan pattern. TSIG generates simulated images at the CCD level for each camera by querying star locations from the TESS input catalog and star images from a realistic PSF image database. The noise processes included in this simulation include background noise (galactic and ecliptic), shot noise, dark current, readout noise, flat field, smear, and saturation. The images are converted into the appropriate format before being used as inputs to the camera simulators, hardware units that were developed to emulate the flight camera electronics, including their interfaces to the ADHU. The ADHU processes the images sent through the camera simulators, computes the centroids of the guide stars using a precomputed pixel list and consequently an error quaternion based on the predicted and measured guide-star centroid positions. The error quaternions information is saved in the fine-pointing packets, which can be processed for analysis. We compare the quaternions in the fine-pointing packets of each camera with the corresponding “truth” input quaternions, computed from the input spacecraft quaternion as shown in Eqs. (5) and (6), where  $dq_{cam}$  is the camera quaternion error,  $q_{sc2cam}$  is the spacecraft to camera quaternion, and  $dq_{sc}$  is the input spacecraft quaternion error. This equation effectively converts the error quaternions in the spacecraft frame to the error quaternions in the camera frame, given the relative orientation of the spacecraft and camera coordinate systems.

$$dq_{cam} = q_{sc2cam}^{-1} \otimes dq_{sc} \otimes q_{sc2cam}, \quad (5)$$

where

$$q_{cam} = q_{sc} \otimes q_{sc2cam}. \quad (6)$$

### 3.2 Attitude Knowledge in Fine-Pointing Acquisition

In this section, we assess the attitude determination capability of the instrument over a wide range of attitude offsets within 120 arc sec, which represents the  $3\sigma$  pointing error in coarse pointing mode. The mission pointing accuracy requirement in this condition is 20 arc sec, which was specified to enable efficient coarse-fine pointing hand-off. In this test, we use a spiral scan pattern to assess the performance of the ADHU software. The spiral scan pattern was selected because it provides a gradual change in radial distance while sampling different  $x$  and  $y$  positions. In addition, the spiral scan possesses a clear

Table 2 Proximity filtering parameters for guide stars.

Parameter	Value
Proximity to bright objects	17 pixels in radial distance
Proximity to variable stars	7 pixels in radial distance
Proximity to saturated objects	15 pixels in row, $N + 15$ pixels in column <sup>a</sup>
Proximity to edge of CCDs	15 pixels in row and column
Proximity to straps	15 pixels in row and column

<sup>a</sup> $N$  is a function of the neighbor star’s magnitude.

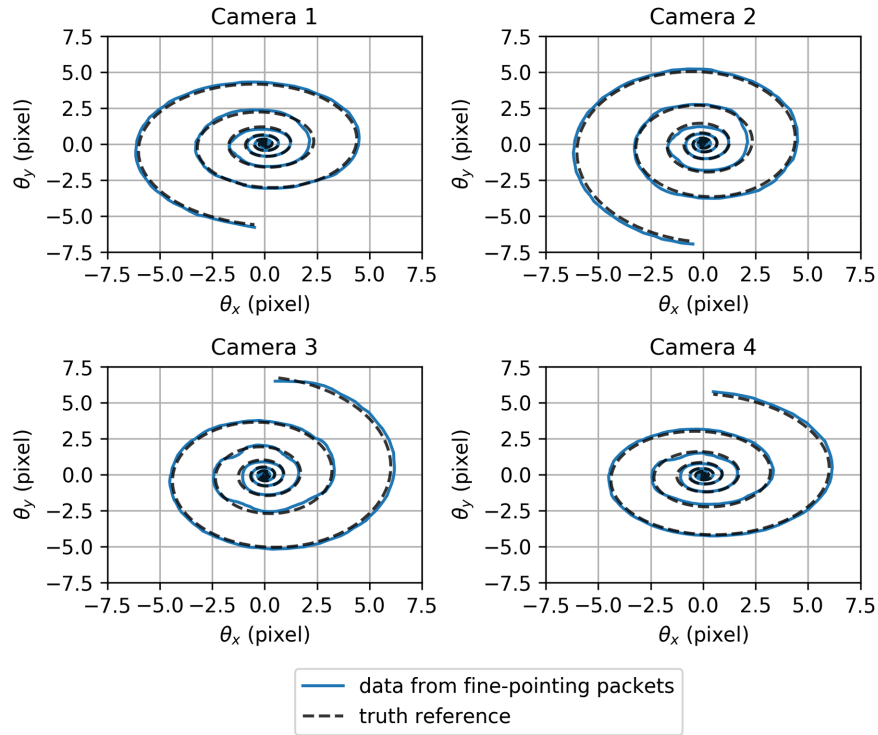


Fig. 5 Spiral scan results from all four cameras along with the corresponding “truth” references.

directionality for easy detection of any rotational inconsistencies in the software implementation.

Figure 5 shows the results from the fine-pointing packets for each camera along with the corresponding “truth” reference, where  $\theta_x$  and  $\theta_y$  represent the rotations about the X and Y axes in the camera frame, converted to pixel units (1 pixel is equivalent to 21 arc sec). Note that, cameras 1 and 2 are mounted at 180-deg offset in the roll direction relative to cameras 3 and 4. The  $3\sigma$  angular errors between the estimated and true attitude in this test are shown in Table 3. It can be seen that for all four cameras, the attitude knowledge requirement of 20 arc sec is met with significant margin.

### 3.3 Attitude Knowledge in Nominal Fine-Pointing Conditions

To test the attitude determination accuracy during nominal fine-pointing conditions, we used an input quaternion series that captures major disturbance sources on the spacecraft platform during fine-pointing. As further explained in Sec. 4, the spacecraft dynamics are primarily driven by reaction wheel readout noise and are not sensitive to instrument guide-stars’ centroids. For this reason, the spacecraft disturbance time series can be used in this test to assess the performance of the instrument’s quaternion estimation algorithm under nominal vibration conditions.

Table 3 Attitude determination error ( $3\sigma$ ) of the cameras in spiral test.

Camera 1	Camera 2	Camera 3	Camera 4	Requirement
4.3 arc sec	5.2 arc sec	5.1 arc sec	4.6 arc sec	20 arc sec

Figure 6(a) shows the true camera quaternion time series (black, dashed line) and the corresponding instrument quaternion time series (blue) for camera 4 for 400 s at an arbitrary observation sector. The X, Y, and Z data represent the rotation about each camera axis, as computed from the quaternion vector components. The “truth” camera quaternion time series are computed from the input spacecraft quaternion time series as previously described in Eq. (5). Figure 6(b) shows the difference between the true camera quaternions and the estimated quaternions by the instrument, along with the  $3\sigma$  requirements for each axis. The  $3\sigma$  quaternion error results for all cameras for the same observation sector are summarized in Table 4. The intermediate centroid errors are also recorded and are within the expected range, in which the spacecraft dynamics are driven by reaction wheel noise. The results of this analysis show that the attitude knowledge requirements during nominal fine-pointing are met for all camera axes with margins.

## 4 Closed-Loop Fine-Pointing Performance

To assess the closed-loop fine-pointing performance, we use the dynamic spacecraft simulator (DSS) provided by Orbital ATK, which simulates the spacecraft dynamics and environmental disturbances. In fine-pointing mode, the DSS receives a commanded quaternion from the quaternion simulator and outputs an actual quaternion of the spacecraft along with spacecraft velocity information. The quaternion simulator computes the updated guide-star positions based on the information from the DSS and guide-star parameters and estimates a new quaternion error, which is passed back to the DSS to complete a closed-loop system. The quaternion simulator is a simplified instrument simulator with quaternion estimation algorithm identical to the flight software. The main difference between the use of the quaternion simulator and the flight software suite is that the quaternion simulator computes the expected guide-star position

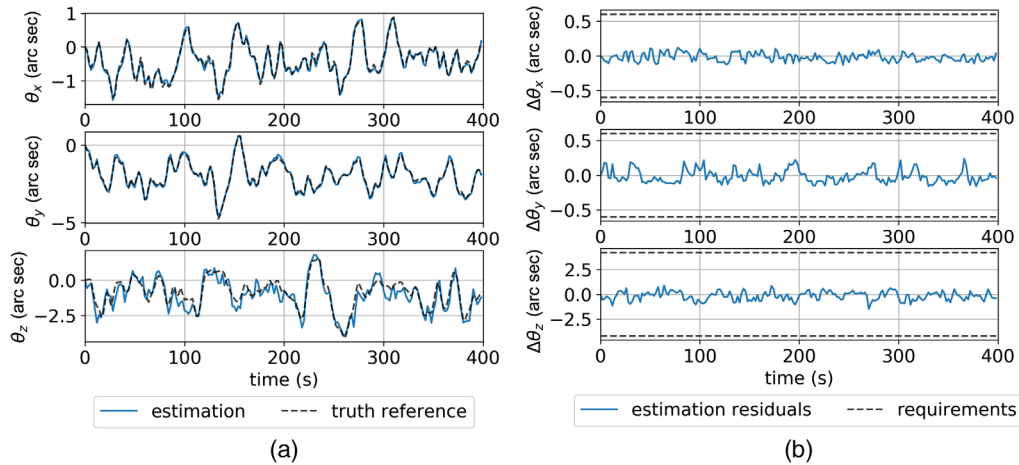


**Fig. 6** Attitude determination performance of the instrument in fine-pointing mode for camera 4 at an arbitrary observation sector (a) quaternion time series estimated by camera 4 (blue) along with the truth reference camera quaternions (black, dashed line), (b) residuals between quaternions estimated by camera 4 and truth reference quaternions along with the corresponding requirements (black, dashed line).

**Table 4** Attitude determination errors ( $3\sigma$ ) for all cameras in sector 1 under nominal fine-pointing conditions.

	$3\sigma$ attitude knowledge error		
	X	Y	Z
Camera 1	0.28 arc sec	0.34 arc sec	1.71 arc sec
Camera 2	0.20 arc sec	0.42 arc sec	2.06 arc sec
Camera 3	0.33 arc sec	0.31 arc sec	1.49 arc sec
Camera 4	0.19 arc sec	0.28 arc sec	1.41 arc sec
Requirement	0.60 arc sec	0.60 arc sec	4.20 arc sec

analytically based on spacecraft motion with the addition of Gaussian noise to account for centroid errors, instead of computing the guide-star centroids from star field images as in the case of flight software. The quaternion simulator was used to avoid star-field image generation at each time step, reducing the computational complexity of the simulation. The simulation was run with scenario scripts written in Orbital ATK's MAESTRO language. The testing framework is shown in Fig. 7. In this analysis, we run both short (24 h) and long (27 days) duration nominal operation scenarios as well as the camera-unavailability due to stray light scenario. In addition, we conduct a sensitivity analysis of the closed-loop performance with respect to the instrument performance in the short duration case to understand the limiting factors in the overall fine-pointing performance.

#### 4.1 Short Duration (24 H)

We collect data at 5 Hz using the framework shown in Fig. 7 for 24 h and compute the power spectral density (PSD) of the time series to reveal the frequency content of the system's dynamics. The pointing jitter levels about the spacecraft axes results are shown in Fig. 8. (The spacecraft axes are shown in Fig. 1).

It can be seen that there is a slow-drift component, primarily about the Y axis in this case. This is caused by velocity aberration, which will be further discussed in Sec. 4.2. The spikes at  $\sim 0.5$  and  $1.8$  Hz represent the effects of the vibrational modes of the solar panels. To assess the system's performance relative to the stability requirements, we compute the forward-sum PSD, integrating from the lowest frequency to a frequency of interest  $f$ , which represents the total energy contained in frequencies lower than  $f$ . The forward-sum PSD is an estimate of the variance  $\sigma^2$  of the data averaged at a time scale of  $T = 1/f$  (noise components with frequencies higher than  $f$  are removed). This analysis is relevant to TESS as the photometry science data are binned in the time domain to longer cadences to facilitate exoplanet detection. The  $3\sigma$  pointing jitter about the spacecraft axes is shown in Fig. 9, along with the corresponding requirements. Since the requirements are relative to the aberrated star field, the slow drift components due to velocity aberrations are not included in the integrated jitter data shown in Fig. 9. The dashed lines show the stability requirements for data averaged over 1-h and 1-min time scales, which were both satisfied by the fine-pointing stability performance in this analysis. Any additional low-frequency residual deviation in the photometry data can be removed in postprocessing through detrending methods. Table 5 shows the  $3\sigma$  pointing jitter values for data averaged at multiple relevant time scales.

A sensitivity analysis was conducted by varying the Gaussian noise level on each guide-star centroid in the quaternion simulator. Figure 10 shows the 2-s and 1-min jitter ( $3\sigma$ ) with a range of guide-star centroid errors ( $1\sigma$ ). The results show that the jitter level does not change relative to centroid error for error levels below 0.1 pixel, which is achieved in most nominal cases. (The average  $1\sigma$  centroid error of a 9th magnitude star under nominal spacecraft disturbances and background noise sources is  $\sim 0.07$  pixel.) Extensive testing and analysis by Orbital ATK has established that the limiting factor of the closed-loop fine-pointing performance is the reaction wheel readout noise. The jitter level about each of the body axes is dependent on the mounting directions of the reaction wheels in the body frame. Since the simulation output is not sensitive to the instrument performance, the data collected from this simulation are representative of the spacecraft dynamics under nominal spacecraft

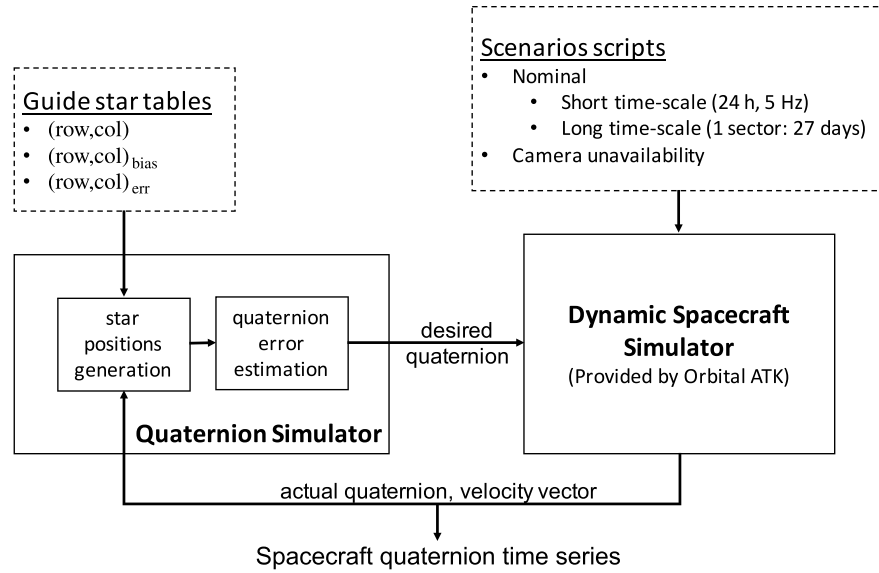


Fig. 7 Closed-loop fine-pointing assessment framework.

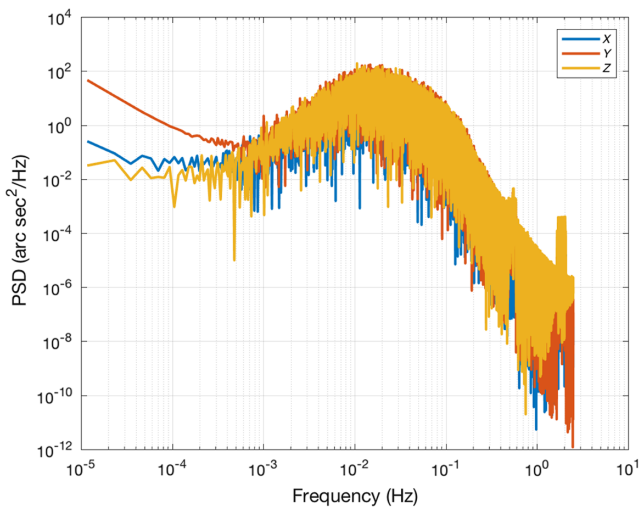


Fig. 8 PSD of fine-pointing data logged from the DSS for 24 h at 5 Hz.

and environmental disturbances and used in Sec. 3.3 to assess the instrument’s attitude determination performance during fine-pointing mode.

#### 4.2 Long Duration (27 Days)

The spacecraft pointing relative to inertial space exhibits a drift behavior in the longer time scales, as seen in Fig. 8, due to differential velocity aberration. Velocity aberration is caused by the relative motion between the observation platform and distant stars, causing aberrations in the stars’ observed positions. In the case of TESS, due to the combined velocity of the spacecraft around the Earth and the velocity of the Earth around the Sun, the apparent guide-star positions as observed by the instrument cameras are aberrated. Since the TESS fine-pointing system relies solely on the guide-star positions for attitude determination, the spacecraft will slowly drift over the span of the orbit to follow the average movement of the star field. To reduce the

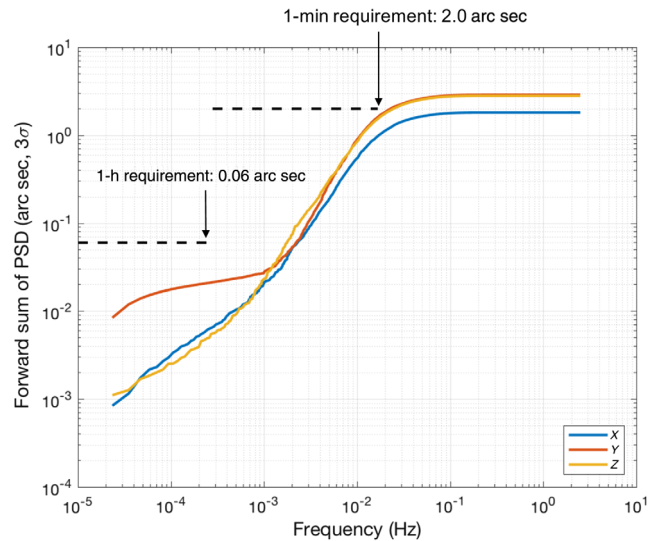
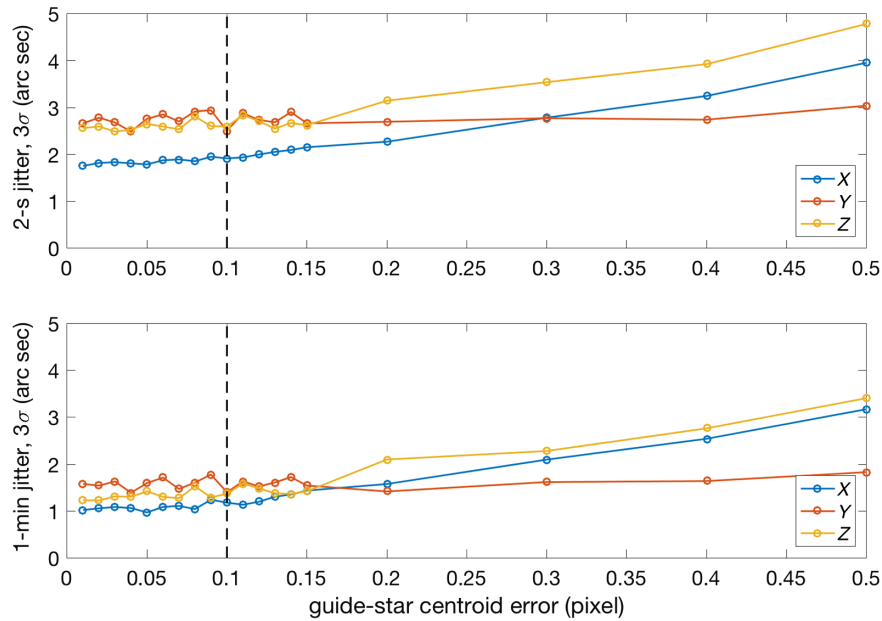


Fig. 9 Fine-pointing stability performance ( $3\sigma$ ) based on the forward-sum of the PSD.

Table 5 Closed-loop fine-pointing stability ( $3\sigma$ ) for relevant time scales.

Time-averaged duration	$3\sigma$ forward-sum PSD (arc sec)			Stability requirement
	X	Y	Z	
2 s	1.81	2.88	2.80	
1 min	0.98	1.60	1.53	2.0 arc sec
30 min	0.011	0.024	0.011	
1 h	0.0065	0.021	0.0056	0.06 arc sec



**Fig. 10** Sensitivity results for 2-s and 1-min jitter ( $3\sigma$ ) with respect to changes in guide-star centroid error ( $1\sigma$ ).

amount of drift over the observation sector, new guide-star tables are uplinked to the spacecraft in LAHO at perigee to be used for the following orbit. The guide-star tables are generated to minimize drift at apogee.

Figure 11 shows the simulated fine-pointing results for 27 days (two orbits) for an arbitrary pointing sector. The results show that the total drift during science operations (HASO) is within  $\pm 2$  arc sec relative to the nominal pointing at apogee. The direction and magnitude of drift vary over time as a function of the spacecraft velocity vector in the Sun-centered frame and the cameras' boresights in inertial space. Due to the mounting configuration of the cameras, the spacecraft experiences higher drift about the cross-axes ( $X$  and  $Y$ ) and lower drift in roll ( $Z$  axis). It is noted that the slow pointing drift effects on science data can be significantly mitigated through detrending methods.

### 4.3 Camera-Unavailability Scenario

Since the TESS cameras cover a wide field of view and are highly sensitive, the Earth and the Moon will often appear close to or in the field of view of a camera, causing the camera to be unusable for guidance. These events occur a few times every sector and last from a few hours to multiple days. When a camera is unusable for guidance, the validity flag of this camera is set to invalid and the information from the camera's fine-pointing packets is not used by the spacecraft's ADCS. A shift in attitude is expected when a camera is not used because of the differences in the aberrated star fields observed by the cameras. To simulate the effect of losing a camera, we start by running the closed-loop simulation in a nominal condition and proceed to turn off camera 1 manually for a period of 4 h before turning the camera back on. The pointing profile

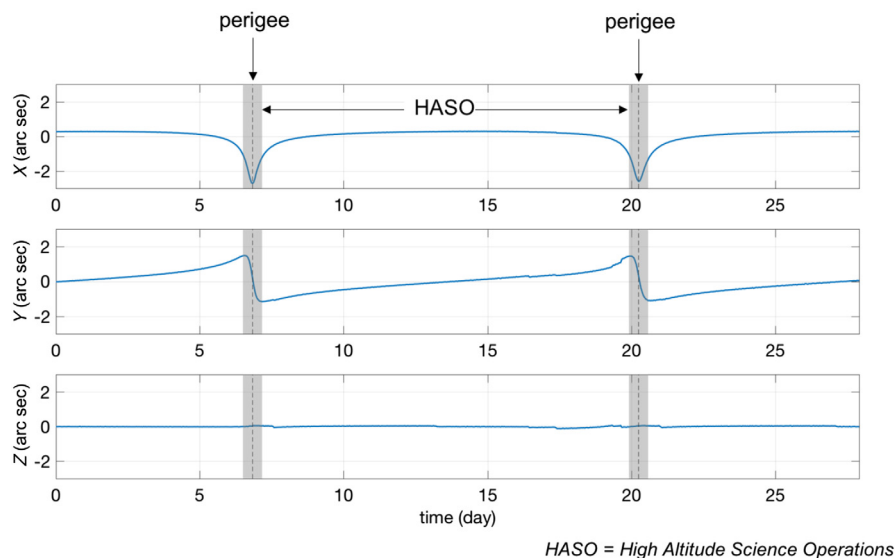


**Fig. 11** Pointing profile of the spacecraft over a span of 27 days (two orbits).

recorded is shown in Fig. 12, where pointing data has been binned at 1 h. It can be seen that losing camera 1 causes a shift of  $<0.05$  arc sec about the  $X$  and  $Z$  axes in this case. Since the shift induced by a camera-unavailability scenario is dependent on velocity aberrations of the guide stars in each camera, the magnitude and direction of shift vary as a function of the orientation of the camera during a specific observation sector and the motion of the spacecraft at the time of camera unavailability. Based on the expected velocity of the spacecraft relative to the Sun over the course of the mission, the pointing shift magnitude could be up to  $\pm 0.2$  arc sec in the worst case scenario. Since these shifts are known events, their effects on photometry data will be mitigated in postprocessing and are not major concerns to planet detection false positives.

## 5 Photometric Precision Assessment

### 5.1 Photometry Simulation and Assessment Framework

We developed a simulation framework, as shown in Fig. 13, to assess the photometric precision of the system in fine-pointing under expected spacecraft jitter and other noise sources. The jitter profile used in this analysis was collected from the DSS at 5 Hz as described in Sec. 4. The PSFs were queried from the same PSF database used for guide-star analysis in Sec. 2.2, where each PSF has a resolution of  $101 \times 101$  points per pixel to provide an ability to model the effects of jitter with high fidelity. Noise sources accounted for in this simulation

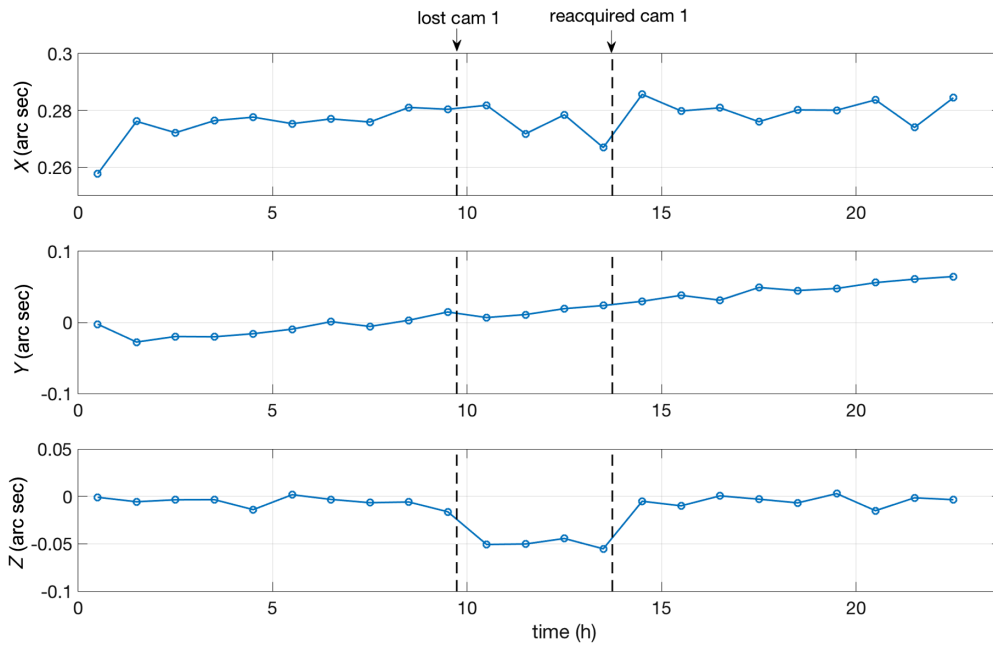


Fig. 12 Pointing profile of the spacecraft in the camera-unavailability and reacquisition scenario.

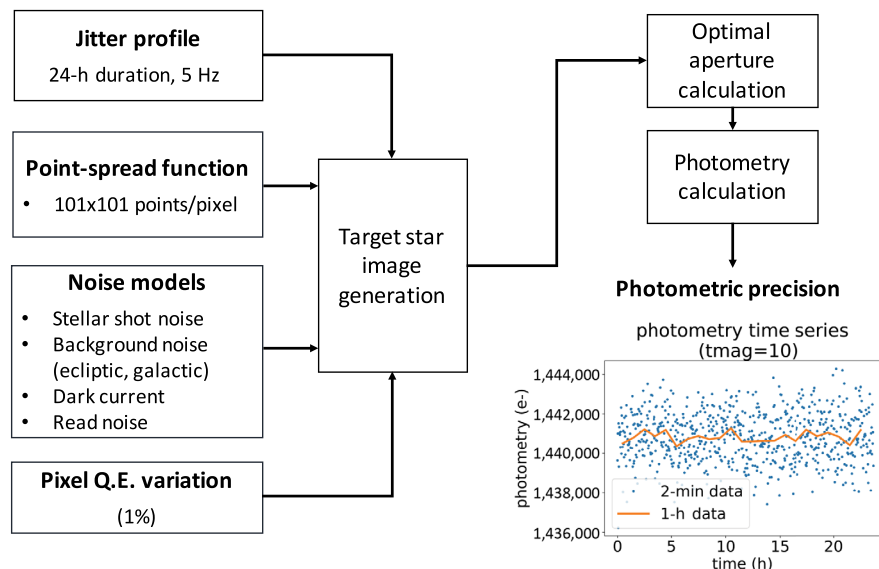


Fig. 13 Overview of the photometry simulation and assessment framework.

include shot noise from the star of interest, background noise (ecliptic and galactic), dark current, and read noise. A CCD quantum efficiency nonuniformity of 1% is also included. These modules are combined to generate simulated images of a target star at a 2-min cadence. An optimal aperture is computed for each simulated target star such that the signal-to-noise ratio of the photometric results is maximized. The photometry data within the optimal aperture for each 2-min cadence are saved for postprocessing. The simulation is run for 24 h and for multiple different star magnitudes and field angles.

The photometric precision of each target star is computed from the raw photometry time series data as follows: (1) background subtraction, (2) time-averaging, and (3) photometric precision calculation. We implemented background subtraction from the raw time series to isolate the photometry signal from only the target star. Since a typical time scale of interest for science objectives is 1 h, the background-subtracted data are then binned at 1-h cadence (average of 30 2-min data points). Finally, the photometric precision is computed as the ratio of the  $1\sigma$  standard deviation and the mean of the 1-h averaged, background subtracted photometry data time series.

## 5.2 Photometric Precision Results

We present the photometric precision in logarithmic scale for target stars of 7th–16th magnitude for five representative field angles in Fig. 14. The error bar on each data point shows the  $1\sigma$  standard deviation in photometric precision of nine independent simulation runs of the same target star with various subpixel offsets relative to the pixel grid. As expected, light curves from dimmer stars are less precise than those from brighter stars due to the decrease in signal-to-noise ratio of the stellar photometry measurement. To further understand the effects of different noise sources on the photometric precision of the target star, Fig. 15 shows the noise contributions to the raw photometric precision of on-axis stars over the same range of magnitudes. It can be seen that the shot noise component is dominant at almost all magnitudes. For faint stars (magnitude > 13), background noise starts to become the dominant noise source. In the mid-range magnitudes (11th to 13th), it can be seen that the jitter-induced photometric noise becomes significant and

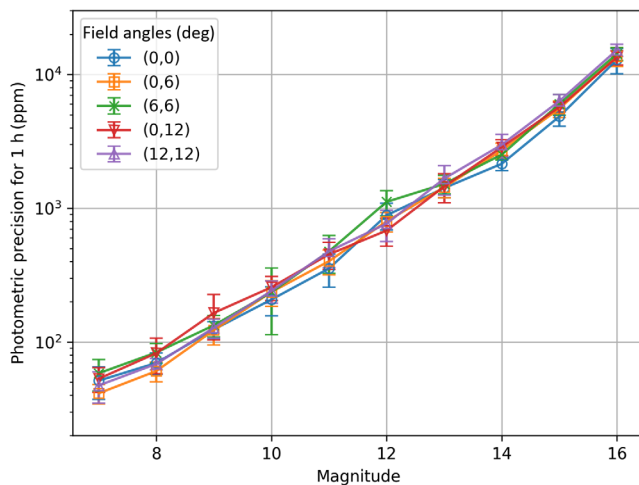


**Fig. 14** Photometric precision (1-h cadence) of 7th to 16th magnitude stars for five representative field angles from raw photometry simulation data (with no additional data processing technique applied).

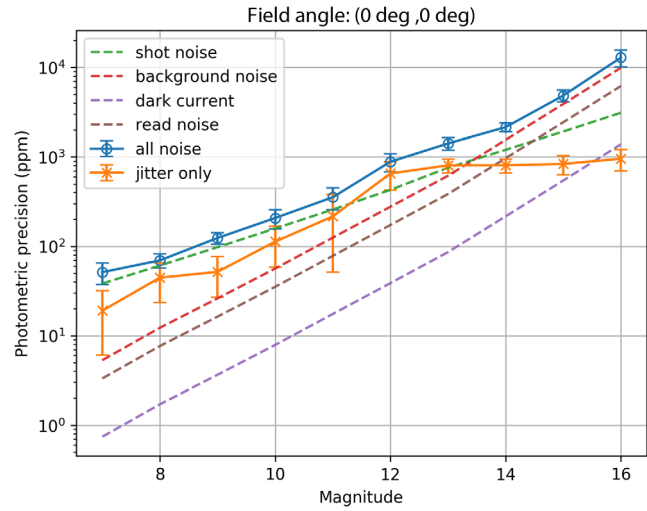


**Fig. 15** Contributions to the raw photometric precision (1-h cadence) from major noise sources for a sample on-axis target star. The total photometric precision of the system can be estimated to be the quadrature sum of the following noise components: stellar shot noise, background noise, dark current, read noise, and pointing jitter.

surpasses shot noise, before leveling off for magnitudes beyond 13th. The jitter curve is highly dependent on the size of the optimal aperture in each case, which becomes smaller with dimmer stars. As jitter causes the light from the target stars to move in and out of the optimal aperture, the smaller the aperture, the more fluctuation the corresponding light curve will suffer due to spacecraft jitter. The plateau occurs when the optimal aperture reaches a minimum number of pixels, in which case, the effect of jitter on the target star reaches a maximum and no longer increases for dimmer stars.

The photometric precision results shown in Figs. 14 and 15 are from raw, unprocessed photometry data. It was shown in the Kepler mission that cotrending techniques are capable of mitigating the effects of systematic noise sources such as pointing jitter on the photometric precision of the system.<sup>12,13</sup> In cotrending methods, independent basis vectors are used to remove systematic, correlated features in data sets. To assess the effect of jitter on science data with basic data processing techniques taken into account, we implemented basic cotrending methods, similar to those used in the Kepler mission.<sup>14</sup> We use a basic least-squares fit cotrending approach using light curves from stars with similar properties to the target star of interest to remove the common systematic effect of pointing jitter on photometry data. Figure 16 shows the raw jitter-induced photometry error for an on-axis star along with cotrended jitter data with light curves from eight other stars. The effects of stellar shot noise and background noise are also shown for reference. The results demonstrate that basic cotrending techniques with light curves from other stars show significant improvement in reducing the effect of jitter on the photometric precision of target stars. The contribution of pointing jitter on photometric precision is estimated to be less than stellar shot noise and background noise at all relevant stellar magnitudes with basic cotrending techniques.

Figure 17 shows the cotrended photometric precision with other similar stars for target stars at five representative field angles within the magnitude range of interest. The required systematic photometric noise limit of 60 ppm and the 30 ppm allocated for pointing jitter (both for stars brighter than 8th magnitude at 1-h cadence) are shown for reference. The results

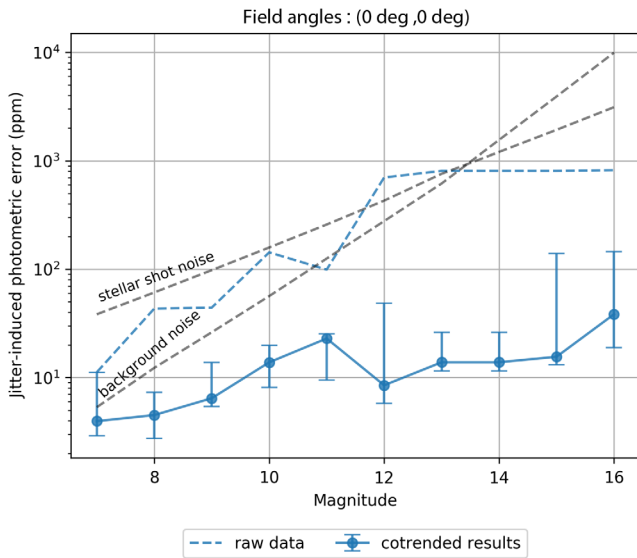


**Fig. 16** Jitter-induced photometric error (1-h cadence) of an on-axis target star before and after cotrending with eight other stars.

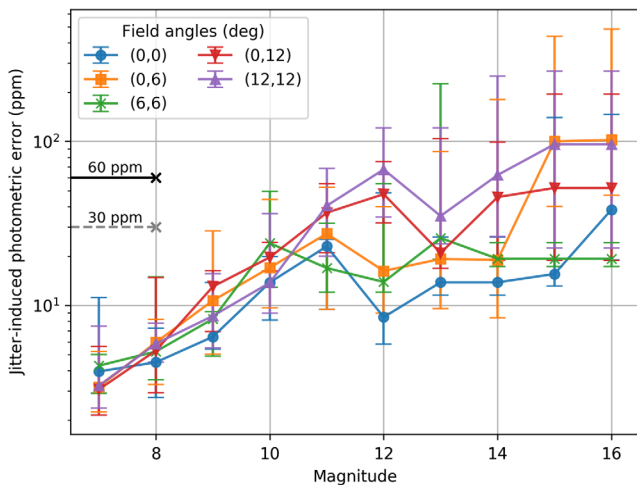


**Fig. 17** Jitter-induced photometric error (1-h cadence) of target stars at representative field angles with the application of co-trending with eight other similar stars.

**Table 6** TESS fine-pointing requirements and expected performance summary.

Fine-pointing assessment parameter	Requirement ( $3\sigma$ )	Expected performance ( $3\sigma$ )
Acquisition accuracy	20 arc sec	<6 arc sec
Nominal accuracy	Pitch, yaw	0.6 arc sec
	Roll	4.2 arc sec
Nominal stability	Per hour	0.06 arc sec
	Per minute	2.0 arc sec

demonstrate that, with basic cotrending techniques, the average photometric error contributed by spacecraft jitter is <30 ppm for stars brighter than 10th magnitude and <100 ppm for stars brighter than 16th magnitude at representative field angles. These results indicate that spacecraft jitter is not a limiting factor in achieving the photometric precision necessary for science objectives and that the photometric precision of TESS will be shot-noise limited for the magnitude range of interest with background noise becoming dominant for faint stars (magnitude > 13).

## 6 Conclusion

In this paper, we present a framework for estimating the fine-pointing performance and the effects of pointing errors on the photometric precision of TESS. The results show that the fine-pointing system is expected to meet all relevant pointing requirements. The instrument cameras are capable of providing attitude knowledge accuracy of <6 arc sec during initial acquisition. In nominal fine-pointing conditions, each instrument camera is expected to provide attitude knowledge accuracy of <0.4 arc sec about the cross axes and <2.0 arc sec about the roll axis. The closed-loop fine-pointing performance with the spacecraft in the loop is estimated to be <2.0 arc sec per minute and <0.03 arc sec per hour. The expected fine-pointing performance and corresponding requirements are summarized in Table 6. With this expected fine-pointing performance, the effects of pointing jitter is determined to be a minor contribution to the system’s photometric precision (<30 ppm for a 10th magnitude star) with basic cotrending techniques.

With the recent launch of TESS, we plan to use on-orbit data to further assess the system’s performance and the validity of the preflight testing framework. The mission is currently in the commissioning phase, where multiple on-orbit experiments are being conducted to acquire relevant postlaunch parameters, which will be used to update the existing models and analyses, and to further improve the system’s performance. The methods and results presented in this paper serves as references in commissioning to ensure optimal system performance.

## Acknowledgments

The authors would like to acknowledge the help and support from the TESS team members at the MIT Kavli Institute of Astrophysics and Space Research, MIT Lincoln Laboratory, Orbital ATK, NASA Goddard Space Flight Center, and NASA Ames Research Center. This graduate research project was supported by the National Science Foundation Graduate Research Fellowship Grant No. 1122374.

## References

- G. R. Ricker et al., “Transiting Exoplanet Survey Satellite,” *J. Astron. Telesc. Instrum. Syst.* **1**(1), 014003 (2014).
- G. R. Ricker et al., “The Transiting Exoplanet Survey Satellite,” *Proc. SPIE* **9904**, 99042B (2016).
- J. J. Lissauer, R. I. Dawson, and S. Tremaine, “Advances in exoplanet science from Kepler,” *Nature* **513**(7518), 336 (2014).
- P. W. Sullivan et al., “The Transiting Exoplanet Survey Satellite: simulations of planet detections and astrophysical false positives,” *Astrophys. J.* **809**(1), 77 (2015).
- J. W. Gangestad et al., “A high Earth, lunar resonant orbit for lower cost space science missions,” arXiv:1306.5333 (2013).
- V. Suntharalingam et al., “Scientific, back-illuminated CCD development for the transiting exoplanet survey satellite,” *NASA Technical Reports Server* (2015).

7. NASA Goddard Space Flight Center, “TESS: Transiting Exoplanet Survey Satellite,” <https://tess.gsfc.nasa.gov> (2018-03-05).
8. “TESS Instrument Requirements Document (IRD) Level 3 Requirements Rev. D,” Unpublished document, MIT Lincoln Laboratory (2015).
9. “TESS Allocations Reference Document (ARD),” Unpublished document, NASA Goddard Space Flight Center (2016).
10. A. Levine, “Fitting star centroids to get Euler angles,” Unpublished technical memo, MIT Kavli Institute of Astrophysics and Space Research, Cambridge, Massachusetts (2015).
11. D. F. Woods et al., “The TESS camera: modeling and measurements with deep depletion devices,” *Proc. SPIE* **9904**, 99042C (2016).
12. M. C. Stumpe et al., “Kepler presearch data conditioning I: architecture and algorithms for error correction in Kepler light curves,” *Publ. Astron. Soc. Pac.* **124**(919), 985–999 (2012).
13. J. C. Smith et al., “Kepler presearch data conditioning II: a Bayesian approach to systematic error correction,” *Publ. Astron. Soc. Pac.* **124**(919), 1000–1014 (2012).
14. J. D. Twicken et al., “Presearch data conditioning in the Kepler Science Operations Center pipeline,” *Proc. SPIE* **7740**, 77401U (2010).

**Tam Nguyen** holds a doctoral degree in space systems from the Massachusetts Institute of Technology. She worked on the TESS fine-pointing system and its impact on the photometric precision of the mission for her doctoral research. She was a graduate student in the MIT Department of Aeronautics and Astronautics and the MIT Kavli Institute for Astrophysics and Space Research, a National Science Foundation graduate research fellow, and an Amelia Earhart fellow.

**Edward Morgan** is a research scientist at the MIT Kavli Institute for Astrophysics and Space Research. He has been working on TESS for the past 5 years and worked on the Rossi X-ray Timing Explorer (RXTE) mission for more than 20 years.

**Roland Vanderspek** is a principal research scientist at the MIT Kavli Institute for Astrophysics and Space Research. He serves as the deputy principal investigator and Science Operations Center lead for TESS. He was deputy project scientist and mission operations manager for the high-energy transient explorer (HETE-2).

**Alan Levine** is a principal research scientist at the MIT Kavli Institute for Astrophysics and Space Research.

**Miranda Kephart** worked on the ground systems software for the TESS mission. She is currently a software engineer at Google.

**James Francis** is an embedded systems software developer, currently responsible for the TESS instrument flight software. He was responsible for the RXTE experiment data system flight software, the Chandra Imaging Spectrometer (ACIS) instrument flight software, and software components on the re-flight of the High Energy Transient Explorer (HETE-2).

**Joseph Zapetis** was a flight software engineer for the TESS mission. He is currently a senior software engineer at Aurora Flight Sciences.

**Kerri Cahoy** is an associate professor of aeronautics and astronautics at the Massachusetts Institute of Technology. She leads the MIT Space, Telecommunications, Astronomy, and Radiation (STAR) Lab, part of the Space Systems Laboratory, and currently holds the Rockwell International Career Development Chair.

**George Ricker** is the principal investigator for the TESS Explorer mission. He is currently the director of the Detector Laboratory and senior research scientist at the MIT Kavli Institute for Astrophysics and Space Research.